



X-ray computed tomography for flame-structure analysis of laminar premixed flames

Emeric Boigné^a, Priyanka Muhunthan^a, Danyal Mohaddes^a, Qing Wang^a, Sadaf Sobhani^a, Waldo Hinshaw^b, Matthias Ihme^{a,*}

^a Department of Mechanical Engineering, Stanford University, Stanford, CA 94305, USA

^b Department of Radiology, Stanford University, Stanford, CA 94305, USA

ARTICLE INFO

Article history:

Received 17 August 2018

Revised 1 October 2018

Accepted 16 November 2018

Available online 28 November 2018

Keywords:

Combustion diagnostics

X-ray radiography

X-ray computed tomography

Premixed flames

Absorption measurements

ABSTRACT

Quantitative X-ray computed tomography (XCT) diagnostics for reacting flows are developed and demonstrated in application to premixed flames in open and optically inaccessible geometries. A laboratory X-ray scanner is employed to investigate methane/air flames that were diluted with krypton as an inert radiodense tracer gas. Effects of acquisition rate and tracer gas concentration on the signal-to-noise ratio are examined. It is shown that statistically converged three-dimensional attenuation measurements can be obtained with limited impact from the tracer gas and within an acceptable acquisition time. Specific aspects of the tomographic reconstruction and the experimental procedure are examined, with particular emphasis on the quantification of experimental uncertainties. A method is developed to determine density and temperature from the X-ray attenuation measurements. These experiments are complemented by one- and multi-dimensional calculations to quantify the influence of krypton on the flame behavior. To demonstrate the merit of XCT for optically inaccessible flames, measurements of a complex flame geometry in a tubular confinement are performed. The use of a coflow to provide a uniform tracer-gas concentration is shown to improve the quantitative temperature evaluation. These measurements demonstrate the viability of XCT for flame-structure analysis and multi-dimensional temperature measurements using laboratory X-ray systems. Further opportunities for improving this diagnostic are discussed.

© 2018 The Combustion Institute. Published by Elsevier Inc. All rights reserved.

1. Introduction

Non-intrusive measurements of flames are critical for obtaining fundamental understanding of flame structure, controlling combustion processes, and guiding the design of novel combustion concepts. Recent developments of multi-dimensional measurements in the form of planar and 3D imaging techniques have greatly contributed to these advances. In particular, optical computed tomography (CT) techniques have provided new opportunities for 2D and 3D flame visualizations. These techniques include laser absorption [1–3], chemiluminescence [4,5] and Schlieren methods [6,7], in which 2D and 3D flow-field representations are generated through the tomographic reconstruction of projection measurements taken at different viewing angles. Although these CT-techniques have been used for examining flame dynamics, exhaust-gas emissions, and turbulence/flame interactions, they introduce technical challenges in terms of optical depth, beam-steering effects, and number of viewing angles. In addition, the

requirement for optical access restricts the utilization of these techniques from applications to complex and confined geometries. X-ray absorption techniques in the form of radiography or computed tomography offer opportunities for overcoming these challenges by providing enhanced solid penetration. As such, X-ray absorption can complement existing optical diagnostic methods by enabling measurements in optically inaccessible environments, such as confined combustors, high-pressure enclosures, or porous media burners.

X-ray absorption measurements in multiphase, inert, and reactive flows have been performed using laboratory and synchrotron sources [8]. Synchrotron sources have the advantage of having a significantly higher photon flux, monochromatic energy beam, and high spatial resolution, but come with the challenge of limited beam-time access, complex operational infrastructure, and restrictive narrow beam cross sections. In contrast, laboratory sources are readily accessible, relatively simple to operate, and provide a large field of view. However, they are limited by having a low photon flux, a limited spatial resolution, and a complex energy spectrum.

Synchrotron X-ray radiography has been employed to examine atomization and spray-dynamics in liquid fuel injectors

* Corresponding author.

E-mail address: mihme@stanford.edu (M. Ihme).

[9–11] and to investigate scalar mixing in turbulent jets [12]. More recently, X-ray fluorescence experiments have been performed to obtain quantitative measurements of density fields in turbulent shear-coaxial jet flames [13], sampling-probe perturbations [14], and heated miniature reactors [15], demonstrating the feasibility of using krypton and argon as fluorescent species. Laboratory X-ray sources have been employed for tomographic imaging of in-situ combustion for oil recovery [16], for probing the spray structure in a full-cone atomizer [17], for investigating the scalar mixing in turbulent jets [18], and for examining the interstitial flame structure and temperature field in porous media burners [19].

This contribution seeks to evaluate the capability of using a laboratory XCT system as an affordable experimental diagnostics in complex and optically inaccessible combustion environments. More specifically, the main objectives of this work are, first, to systematically quantify X-ray system settings, uncertainties, signal-to-noise ratios, and flow-parameter sensitivities by considering a benchmark flame configuration; second, to investigate the importance of tracer gas uniformity in estimating gas density and temperature from X-ray absorption and to identify sources of signal fluctuations; third, to conduct quantitative comparisons of XCT-absorption measurements with results from multi-dimensional numerical simulations; fourth, to extend this analysis by considering a geometrically complex flame that is confined within a solid structure; and, lastly, to discuss opportunities for further improving this XCT diagnostic.

The remainder of this paper has the following structure. XCT-theory in the context of reacting flow diagnostics is given in Section 2. The experimental setup is presented in Section 3. Results focusing on the calibration, uncertainty analysis, effects of operating conditions on the flame structure and comparisons with detailed simulation results are discussed in Section 4. Section 5 provides a discussion of potential improvements and limitations, and the paper closes with conclusions in Section 6.

2. Theoretical background

In X-ray imaging, the beam intensity is attenuated by the object due to the interaction of X-ray photons with outer and inner shell electrons by photoelectric absorption, and through inelastic and elastic scattering by Compton and Rayleigh effects [20]. Relaxation of ionized atoms also contributes to the emission of characteristic fluorescent X-rays. Because of the isotropic emission, the large distance between object and detector, and the filtering, the detection of the emitted fluorescence signal was found to be below the detector noise level and is thus neglected. However, corrections can be considered to improve the calibration and to account for effects of fluorescent in the detector calibration. This becomes relevant with increasing spherical detector cap and appreciable low-photon energy emissions. Although not observed in the present setup, we note that fluorescence effects can potentially lead to a loss in spatial resolution as the isotropic fluorescence emission will excite further elastic scattering of the surrounding gas.

The intensity I of a polyenergetic X-ray beam interacting with an object along a path \mathcal{L} is related to its incident intensity I_0 via the Beer–Lambert law [20],

$$I = I_0 \int Q(E) \exp \left\{ - \int_{\mathcal{L}} \mu(E, s) ds \right\} dE, \quad (1)$$

where E is the photon energy, μ is the linear attenuation coefficient of the object (in units of cm^{-1}), s is the path coordinate, and $Q(E)$ is the incident spectral distribution function, dependent on both the energy distribution of the source and the detector spectral function. The linear attenuation coefficient is commonly expressed in terms of density, ρ , and mass attenuation coefficient, ζ (in units

of cm^2/g) as

$$\mu(E, s) = \zeta(E, s) \rho(s). \quad (2)$$

The attenuation coefficients μ and ζ are tabulated quantities that depend on both atomic composition and photon energy [21]. The relative contributions of absorption and scattering are a function of the photon energy, and the photoelectric contribution is dominant in the low energy range. At low energies, this contribution scales as Z^3/E^3 , where Z is the atomic number, and features characteristic sharp increases at photon energies close to the binding energies of inner shell electrons. For higher photon energies, the Compton scattering becomes the predominant absorption effect.

Common detectors used in X-ray imaging, such as the one considered in this work, are energy-integrating detectors that are not able to discriminate between energy levels, fluorescent, scattered, and non-absorbed photons. It is therefore convenient to introduce energy-averaged linear and mass attenuation coefficients $\bar{\mu}(s)$ and $\bar{\zeta}(s)$ such that Eqs. (1) and (2) may be written as

$$I = I_0 \exp \left\{ - \int_{\mathcal{L}} \bar{\mu}(s) ds \right\}, \quad (3a)$$

$$\bar{\mu}(s) = \bar{\zeta}(s) \rho(s). \quad (3b)$$

Variations of the observed spectrum along the different X-ray paths due to preferential absorption of the low energy X-rays are known to result in beam hardening artifacts when operating with energy-integrating detectors [22]. Such artifacts were not observed in this work, and the rest of the analysis will only consider energy-averaged quantities.

By considering a gaseous mixture that consists of N_s species, and introducing the ideal gas law to eliminate the partial density, Eq. (3b) may be written as [19]

$$\bar{\mu} = \frac{p}{R_u T} \sum_{i=1}^{N_s} \bar{\zeta}_i W_i X_i, \quad (4)$$

where p is the pressure, R_u is the universal gas constant, T is the temperature, and W_i , X_i and $\bar{\zeta}_i$ are molecular weight, mole fraction and energy-averaged mass attenuation coefficient of the i th species, respectively. Because of their low absorption cross sections, H, C, N and O atoms that are present in reactant and product species of gas-phase combustion are ineffective in attenuating X-rays at energy levels commonly employed in laboratory systems. Therefore, a tracer gas is required, and the present study utilizes krypton due to its high radiodensity, chemical inertness, and acceptable cost. By only considering Kr as the absorbing medium, Eq. (4) reduces to

$$\bar{\mu} \approx \bar{\mu}_{\text{Kr}} = \bar{\zeta}_{\text{Kr}} \rho_{\text{Kr}} = \frac{p \bar{\zeta}_{\text{Kr}} W_{\text{Kr}} X_{\text{Kr}}}{R_u T}, \quad (5)$$

highlighting that the X-ray attenuation is directly related to the partial density of Kr. By considering an isobaric system, the temperature can then be related to a known reference state as

$$\frac{T}{T_{\text{ref}}} = \frac{X_{\text{Kr}}}{X_{\text{Kr,ref}}} \frac{\bar{\mu}_{\text{ref}}}{\bar{\mu}}, \quad (6)$$

where the subscript ‘ref’ denotes the reference state.

For the condition of constant Kr mole fraction, Eq. (6) provides a direct expression for relating the measured linear attenuation to temperature. However, variations in Krypton mole fraction by entrainment and non-equimolar reactions require consideration in the evaluation of the temperature. By separating both effects and considering a two-stream system, X_{Kr} in Eq. (6) can be written as:

$$X_{\text{Kr}} = X_{\text{Kr}}(T, \xi) = X_{\text{Kr},0}(\xi) + \Delta X_{\text{Kr},\xi}(T), \quad (7)$$

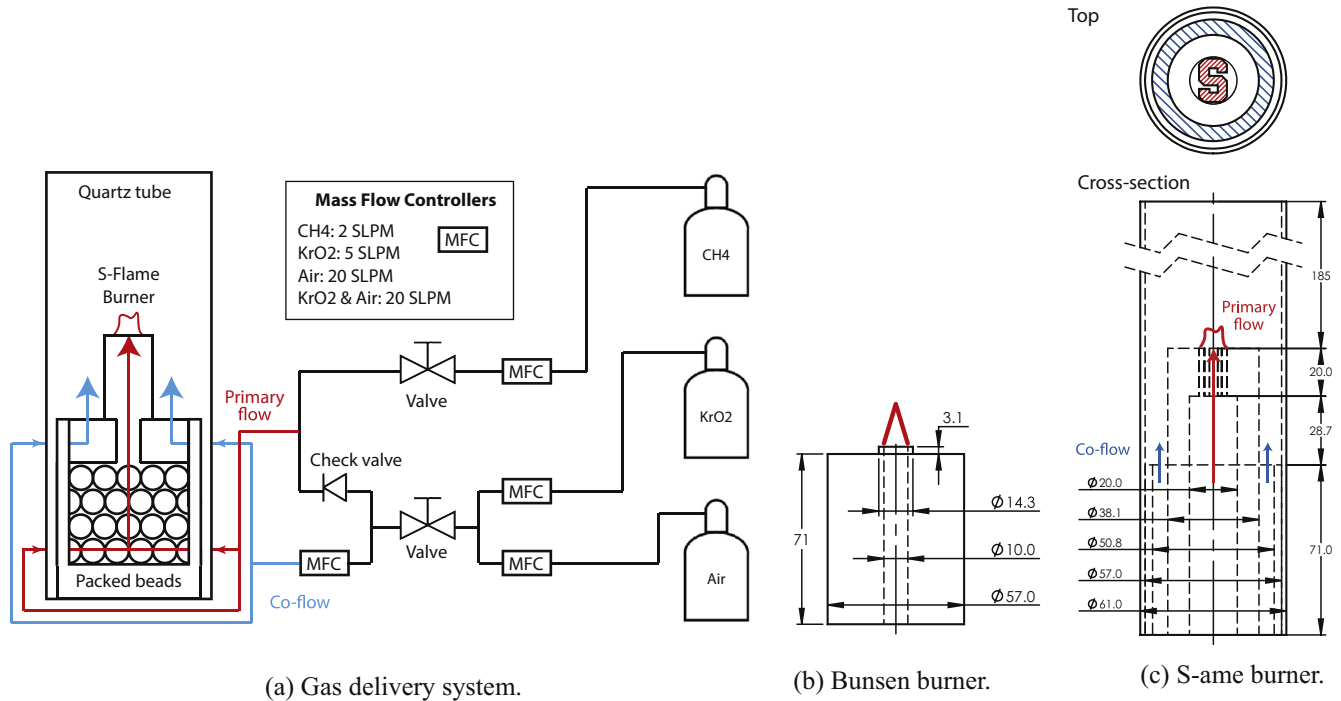


Fig. 1. Schematic of (a) gas delivery system, (b) Bunsen burner, and (c) S-flame burner. Dimensions in mm.

where $X_{Kr,0}(\xi) = (1 - \xi)X_{Kr,1} + \xi X_{Kr,2}$, with ξ being the scalar mixing variable between primary (subscript 1, $\xi = 0$) and secondary stream (subscript 2, $\xi = 1$), $X_{Kr,1}$ and $X_{Kr,2}$ are the initial Kr mole fractions in both streams; $\Delta X_{Kr,\xi}(T)$ represents the variations in Kr mole fraction due to changes in the mean molecular weight by the combustion chemistry. By neglecting effects of variations in X_{Kr} , a so-called inferred temperature T^* is obtained from Eq. (6), which approximates the true temperature T . In the following, both effects will be investigated through theoretical and experimental analysis.

3. Experimental setup

3.1. Burner and flow system setup

X-ray absorption was applied to a modular burner with a coflow that could be operated both with a Bunsen flame and a complex flame in the form of a S-shaped burner exit-profile. The gas delivery system and burner mount are illustrated in Fig. 1a, while dimensions of the Bunsen burner are presented in Fig. 1b. During the operation of the Bunsen flame, the coflow was blocked and the surrounding air was entrained into the jet. The Kr-fuel-air mixture was ejected through a nozzle with a diameter $D = 10$ mm, and was supplied by two opposing radial inlets before passing through a plenum filled with packed beads to ensure complete mixing and to prevent flashback.

To operate the S-flame, a quartz tube was added on top of the burner mount to confine the flow and to prevent entrainment of ambient air. A secondary flow of Kr/O₂ and air was used to provide a nearly constant Kr concentration environment inside the tube. This S-flame setup is illustrated in Fig. 1c.

All experiments were performed with methane (99.7% purity), compressed air (extra-dry grade), and a krypton/oxygen mixture (21% O₂ by volume). The gases were supplied from gas cylinders and metered through mass flow controllers (Alicat Scientific) as represented in Fig. 1a. Based on manufacturer data, error propagation in the operating parameters was calculated. It was deter-

mined that maximum errors in total mass flux, equivalence ratio, and Kr mole fraction did not exceed 2%, 3%, and 4%, respectively. The mixture composition was controlled through a LABVIEW interface. Gases were supplied to the burner using flexible tubing, having been premixed at a junction approximately 200 tube diameters upstream of the burner exit. The burner was mounted using a Newport kinematic base to a precision rotating table (Parker) to ensure spatial repeatability of the burner position to within 5 μ m.

3.2. X-ray system

In this work, X-ray radiography and tomography measurements were performed using a table-top laboratory X-ray system. The setup is schematically illustrated in Fig. 2. This system uses a cone beam X-ray source and consists of a radiography tungsten X-ray tube (Varian G-1593BI with a nominal focal spot size of 0.3 mm and Varian B-180H tube housing), a 100 kW power supply (CPI model Indico 100), a collimator (Huestis Model 150A), and a flat panel detector (Varian 4030CB detector). X-ray photons reaching the detector first pass through a 3.8 mm thick carbon fiber plate and a 0.1 mm thick Al plate, before reaching a cesium-iodide scintillator that is doped with thallium. Besides the ones embedded within the X-ray tube housing (1 mm Al) and the collimator (equivalent of 2 mm Al), no additional beam filter was employed. The filtering employed in this setup significantly reduces the low-energy spectrum of the incoming 14.3 keV photons.

The detector consists of an array of 2048×1536 pixels with a pixel size of 194μ m resulting in a $397 \times 298 \text{ mm}^2$ total pixel area. However, due to the limited detector reading rate, a 2×2 pixel binning mode was used to increase the acquisition rate. This resulted in detected images of 1024×768 pixels at a special resolution of 388μ m. The distances between the source and the center of rotation and between the source and the detector were 626 mm and 1096 mm, respectively. Distances were chosen to maximize resolution with the cone-beam geometric magnification and to ensure sufficient separation between the flame and X-ray components to prevent excessive heating. Tube voltage and tube in-

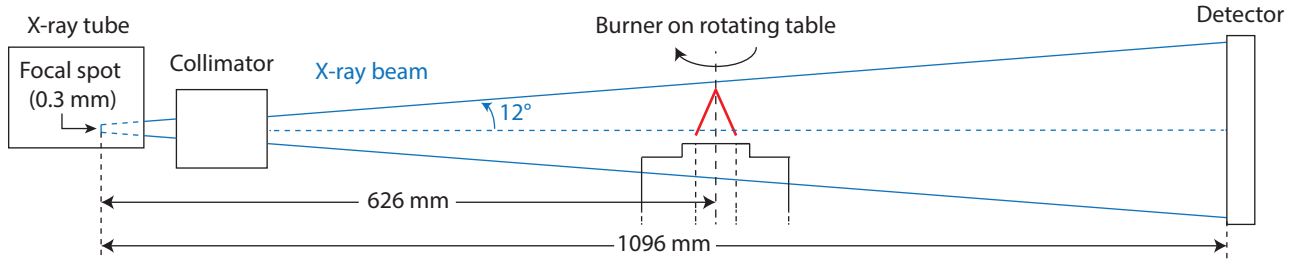


Fig. 2. Schematic of the table-top laboratory X-ray system consisting of a burner mounted on a precision rotating platform with X-ray tube, collimator and detector.

tensity were chosen to maximize signal-to-noise ratio (SNR) for each configuration, and to prevent the saturation of the detector. For the Bunsen flame, a low intensity mode of the X-ray source was used to limit the thermal heating of the tube, allowing longer operating times and thus accumulation of numerous acquisitions. In this mode, the maximum SNR was found with a tube peak voltage of 40 kVp and the corresponding maximum tube current of 40 mA. For the S-flame, the X-ray source was operated in the high-intensity mode allowing a further increase in SNR, but limiting the acquisition period to 10 min before reaching the tube's critical temperature. Due to the presence of the quartz tube around the flame, the maximum SNR was obtained with a tube current of 60 mA, and a tube voltage of 55 kVp providing more penetrating photons.

3.3. X-ray acquisition and experimental procedure

To account for gains and offsets of the detector that are unique to each pixel, a standard X-ray absorption procedure includes a normalization using a set of dark images (acquired without an X-ray beam) and a set of flat images (acquired with an X-ray beam, without an object). With this setup, two additional effects were observed and corrected for: first, a temporal instability and drift of the beam intensity over the duration of a full 360° acquisition, and, second, a blurring of the edges and a spreading of the solid attenuation of up to 10 pixels. To correct for these effects, a modified acquisition procedure was derived, which is described below.

Each acquisition corresponds to a set of 1024 projection images of intensity I , taken at a frequency of 15 Hz over a 360° rotation of the sample. The exposure time was 40 ms per image. The image processing followed three steps: first, the mean of a set of 256 dark images of intensity I_{drk} , taken after every acquisition, was subtracted pixel-wise from each of the 1024 projection images. In the second step, a gain normalization was applied using the mean intensity of a non-attenuated region consisting of 128×128 pixels. Finally, a gain normalization was applied using a set of 1024 flat images of intensity I_{flt} , with the burner in the field of view but without any flow to correct for the blurring and pixel gain. The first and third steps follow standard XCT procedure. The second step was added to correct for observed temporal variations and drift in the beam intensity. X-ray bench-top sources are typically less stable than synchrotron sources, and temporal fluctuations in the intensity of up to 5% were observed before correction. For each of the projection images, the radiography signal $\int_{\mathcal{L}} \bar{\mu}(s) ds$ introduced in Eq. (3a) was then obtained as

$$\int_{\mathcal{L}} \bar{\mu}(s) ds = -\log \left\{ \frac{\langle I - I_{drk} \rangle}{\langle I_{flt} - I_{drk} \rangle} \right\}, \quad (8)$$

where the angular brackets denote the temporal-drift normalization.

The number of flat and projection images acquired was varied depending on the operating conditions, and chosen to maximize the photon count while keeping a reasonable acquisition time. In standard XCT applications, this number is typically chosen by con-

sidering the limit necessary to properly resolve each pixel given the constant rotation of the object. From simple geometric considerations [23], this corresponds to the following lower bound for the number of projections N_p acquired over a 360° CT rotation to ensure pixel overlap between consecutive images

$$N_p > \pi \frac{D}{\Delta}, \quad (9)$$

where D is the largest object diameter, and Δ is the spatial pixel resolution. Given the diameter of the flames considered in this work, this condition is largely respected and N_p was deliberately chosen to increase the quality of the images.

3.4. X-ray computed tomography reconstruction algorithm

From the radiography signal $\int_{\mathcal{L}} \bar{\mu}(s) ds$ obtained from Eq. (8), the 3D attenuation field $\bar{\mu}$ was then obtained by computed tomography. The GPU-implementation of the Feldkamp–Davis–Kress (FDK) algorithm in the ASTRA Toolbox [24,25] was used to reconstruct the 3D field with an isotropic voxel size of 222 μm .

This section further describes the FDK algorithm used to provide a basic understanding of CT techniques to the reader, as well as report on salient choices made on the implementation. The interested reader is referred to the literature for further details on this method [22,26].

The FDK algorithm is widely used in cone beam CT, and is an approximate reconstruction algorithm based on a fan beam reconstruction method. As a first order approximation, which is valid close to the beam centerline, this algorithm relates the projection and reconstructed data linearly, with limited geometric artifacts. In the case of the considered flames, the centerline was placed precisely at the height of the burner exit as shown in Fig. 2. X-ray beams passing through the flame thus had angles below 3° with respect to the beam centerline, limiting the geometric artifacts.

In the limit of small angles, the FDK algorithm converges to the filtered backprojection (FBP) method developed for parallel-beam geometries. The FDK algorithm corresponds to a modified version of the FBP method by weighting the projections as if they had been measured along the beam centerline. To further illustrate how the attenuation field $\bar{\mu}$ of an object can be retrieved from the radiography signal $\int_{\mathcal{L}} \bar{\mu}(s) ds$, the FBP algorithm is described in the following paragraph.

Let us consider a parallel beam configuration, and a planar slice of a rotating object described by an attenuation field $\bar{\mu}(x, y)$ as represented in Fig. 3. This reduces the 3D problem to a 2D one. At a given angle β of the rotating object, the projection of the planar slice results in a 1D shadow function of the object $p_{\beta}(\rho)$, where ρ is the linear coordinate in the detector plane. The Radon transform \mathcal{R} is the mathematical operator obtained when collecting the set of projections over the entire set of possible angles, β , which can be expressed as

$$\mathcal{R}\{\bar{\mu}\}(\rho, \beta) = \int_{\mathcal{L}(\rho, \beta)} \bar{\mu}(s(\rho, \beta)) ds, \quad (10)$$

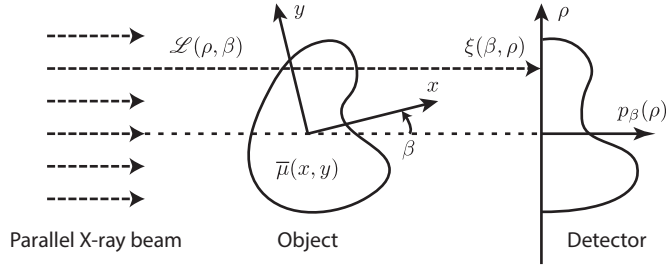


Fig. 3. Schematic of a parallel beam configuration for illustrating the FBP algorithm. The projection profile $p_\beta(\rho)$ on the detector is obtained from the attenuation $\bar{\mu}(x, y)$ of the object along X-ray lines $\mathcal{L}(\rho, \beta)$ at a given angle β of the rotating object.

where s denotes the linear coordinate along the X-ray line $\mathcal{L}(\rho, \beta)$. It is possible to directly invert the Radon transform by using the Fourier-slice theorem that relates the 2D Fourier transform of the attenuation field $\mathcal{F}_{2D}\{\bar{\mu}\}$ to the 1D Fourier transform of the projections $\hat{p}_\beta(\omega) = \mathcal{F}_{1D}\{p_\beta(\rho)\}(\omega)$ of Fourier coordinate ω , as [26]

$$\mathcal{F}_{2D}\{\bar{\mu}\}(\omega \cos(\beta), \omega \sin(\beta)) = \hat{p}_\beta(\omega), \quad (11)$$

By then writing the inverse 2D Fourier transform in polar coordinates, and recognizing the Fourier-slice theorem expression, one retrieves the FBP inversion for the Radon transform

$$\begin{aligned} \bar{\mu}(x, y) &= \mathcal{F}_{2D}^{-1}\{\mathcal{F}_{2D}\{\bar{\mu}\}\}(x, y) \\ &= \int_0^\pi \int_{\mathbb{R}} \underbrace{\mathcal{F}_{2D}\{\bar{\mu}\}(\omega \cos(\beta), \omega \sin(\beta))}_{\hat{p}_\beta(\omega)} \\ &\quad \times \exp[i2\pi\omega(x \cos(\beta) + y \sin(\beta))] |\omega| d\omega d\beta \\ &= \int_0^\pi \underbrace{\mathcal{F}_{1D}^{-1}\{\hat{p}_\beta(\omega)|\omega|\}}_{q_\beta}(x \cos(\beta) + y \sin(\beta)) d\beta \\ &= \mathcal{B}\{q_\beta\}(x, y), \end{aligned} \quad (12)$$

which is compactly written in the last expression using the back-projection operation $\mathcal{B}\{\cdot\}(x, y)$ on the filtered projections q_β . This compact notation highlights the two successive steps of the FBP algorithm: first to filter the projection in Fourier space with a ramp filter $|\omega|$, and second to sum the individual contributions over all angles.

The convolution with the ramp filter amplifies high-frequency noise resulting in significant SNR degradation. Additional filters such as cosine, Hamming, Hanning, or Shepp–Logan are commonly used to reduce this high-frequency noise at the cost of deteriorating the resolution. In order to maintain the maximum resolution possible, no such additional filters were used in the present work. The ramp filter was implemented using a standard rectangular band-limiting window, referred to as a Ram-Lak filter [27].

4. Results

Prior to performing flame measurements, a calibration was performed in order to characterize experimental uncertainties. The effects of Kr dilution on the flame structure as well as effects of variations in Kr mole fraction across the flame on the estimation of gas density and temperature were investigated using 1D simulations of an unstrained laminar premixed flame. A series of measurements were then performed with a Bunsen flame with the specific goals of (i) assessing the capability of the method to retrieve the flame structure over different operating conditions, (ii) investigating the reduction of noise and convergence of the signal by averaging over multiple acquisitions, and (iii) evaluating the feasibility of extracting quantitative results for thermodynamic state variables through

Table 1

Operating conditions considered for the Bunsen flame, reporting jet-exit Reynolds number Re , equivalence ratio ϕ , and Kr mole fraction X_{Kr} . Flame thickness δ_f [μm], burnt temperature T_b [K], and laminar flame speed s_L [cm/s] were evaluated from 1D unstrained flame calculations described in Section 4.2. Flame series A considers variations in Kr mole fraction, flame series B examines effects of equivalence ratio variations and flame C1 is operated to investigate averaging over numerous acquisitions.

Flame	Re	ϕ	X_{Kr}	δ_f	T_b	s_L
A1	655	1.30	0.65	291	2422	51.5
A2	671	1.30	0.55	322	2360	46.3
A3	693	1.30	0.45	357	2299	41.5
A4	719	1.30	0.35	398	2240	37.0
A5	753	1.30	0.25	447	2183	33.0
A6	614	1.30	0.00	633	2054	23.5
B1	415	1.30	0.60	306	2392	48.9
B2	415	1.40	0.60	380	2307	37.3
B3	415	1.50	0.60	512	2220	26.6
B4	416	1.60	0.60	657	2133	20.0
B5	416	1.70	0.60	792	2048	15.9
C1	462	1.40	0.55	407	2276	34.8

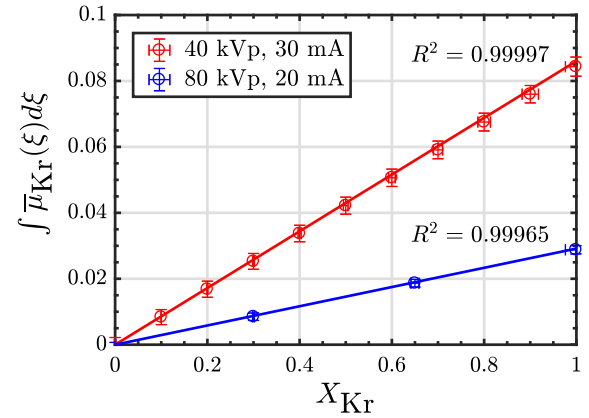


Fig. 4. Calibration curve of mean path-integrated Kr absorption for two X-ray tube settings (energy, in peak kilovoltage (kVp), and current, in mA). Uncertainties in Kr mole fraction are indicated by horizontal error bars. Standard deviations in the signal are indicated by vertical error bars.

comparisons against detailed numerical simulations. To this end, different flame series were considered (see Table 1). The first, denoted flame A, considers variations in X_{Kr} , and the second, denoted flame B, examines effects of equivalence ratio variations. In addition, flame C1 is operated to examine the averaging of numerous acquisitions, N_a .

To demonstrate the applicability of this technique to optically inaccessible and complex flame geometries, a second geometrically more complex and confined flame was considered.

4.1. Experimental calibration

Calibration measurements were performed to characterize the X-ray system. For this, a premixed stream of Kr and air at different molar ratios was supplied to a plastic tube placed on the X-ray rotating table. Calibration results for two settings of the X-ray tube are presented in Fig. 4, showing the mean path-integrated Kr-absorption, for a uniform region of 4884 pixels averaged over 1024 radiography images. The linear regression curves are plotted by solid lines, with R^2 correlation coefficients reported directly on the figure. Uncertainties in the Kr mole fraction, arising from the mass flow controllers, are indicated by horizontal error bars. Vertical error bars denote the standard deviation over the set of pixels considered as an estimate of the SNR. It is observed that the linear attenuation decreases with increasing tube volt-

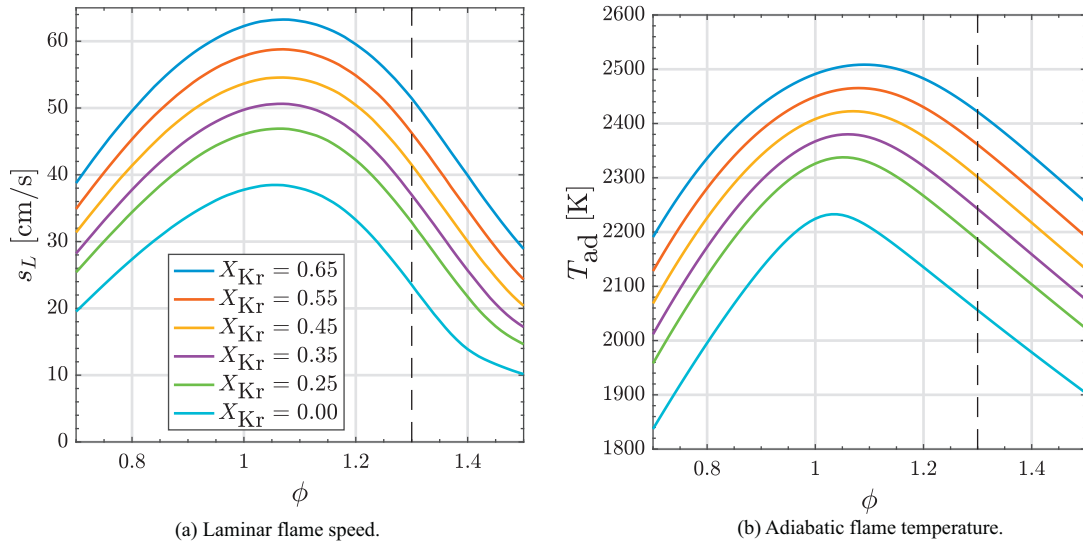


Fig. 5. (a) Laminar flame speed s_L and (b) adiabatic temperature T_{ad} obtained from 1D simulations of unstrained laminar premixed flames performed with CANTERA. The vertical black dashed lines indicate the equivalence ratio of the conditions considered in Fig. 6.

age, in agreement with the known Z^3/E^3 dependency of the photoelectric contribution. From tabulated values of attenuation coefficients [21], the mean energy of the X-ray energy spectrum was evaluated as $\bar{E} = 30.5$ keV for the 40 kVp data. At this energy, the mean mass attenuation and linear attenuation coefficients of pure Kr gas at ambient conditions are evaluated as $\bar{\zeta}_{Kr} = 17.72$ cm²/g and $\bar{\mu}_{Kr} = 0.061$ cm⁻¹, respectively. These values were used for the evaluation of the partial density and inferred temperature from the reconstructed attenuation fields presented in Section 4.3.4.

4.2. Influence of Kr dilution on the flame

In the context of using X-ray absorption measurements to estimate thermodynamic properties of gases, it is crucial to properly characterize potential sources of spatial fluctuations in the Kr concentration. For single-stream systems, the only source of Kr non-uniformity arises from concentration gradients driven by non-equimolar reactions and diffusion across the flame. To examine this effect, 1D simulations of unstrained laminar premixed flames were performed with CANTERA [28]. A modified GRI 3.0-methane reaction mechanism [29] was employed, in which Kr was added as an inert gas, assuming the same collision efficiency as Ar [30]. Computed unstrained laminar flame speeds and adiabatic flame temperatures are reported for different equivalence ratios and Kr concentrations in Fig. 5. Axial profiles for temperature and Kr mole fraction, along with profiles of $X_{Kr}(T)$ are shown in Fig. 6. Flame thicknesses δ_f , burned gas temperatures T_b and laminar flame speeds s_L of the experimentally investigated flames are reported in Table 1. The flame thicknesses were obtained from the spatial temperature profiles presented in Fig. 6a, with δ_f defined as

$$\delta_f = \frac{T_b - T_0}{\max(dT/dx)}, \quad (13)$$

where T_0 is the ambient temperature. These calculations show that increasing the Kr dilution results in an increase in the flame speed and a thickening of the flame. Axial profiles of Kr mole fraction highlight that, due to the formation of intermediate species across the flame, the Kr mole fraction decreases by about 6% for flames in series A, and up to 11% for the richest mixture considered (flame B5, not shown). It is noted that these variations are reduced for stoichiometric and lean flames due to the equimolar nature of the global reaction of methane with air.

In the case of a single-stream system ($X_{Kr,1}(T) = X_{Kr,2}(T)$ in Eq. (7)), the X_{Kr} profiles of Fig. 6c can be employed to determine the temperature profiles taking into consideration variations in the Kr mole fraction through the flame.

4.3. Investigation of an axis-symmetric Bunsen flame

4.3.1. Krypton dilution

Effects of Kr dilution on the X-ray signal and flame behavior are examined experimentally. Flame series A is considered, in which the Kr mole fraction is successively reduced while keeping equivalence ratio and mass flow rate constant. Results of path-integrated radiography signals and tomographic reconstructions of cross sections of $\bar{\mu}_{Kr}$ are shown in Fig. 7. The X-ray radiography results, shown in Fig. 7a, were obtained by averaging over 1024 projection images with a spatial resolution of 388 μ m at the detector. From this set of results, the characteristic conical shape of a Bunsen flame is visible. However, by reducing the Kr concentration, an appreciable degradation in contrast and SNR can be observed. This is particularly evident for flame A5, with the lowest Kr mole fraction of 0.25.

Tomographic reconstructions presented in Fig. 7b show a slightly asymmetric flame shape, which was also observed by chemiluminescence. At this resolution, the flame thickness is resolved by less than four pixels for flame A1. A slight broadening of the reaction zone is observable for flame A2, which is in agreement with 1D simulations. Quantitative differences in flame thicknesses between Table 1 can be explained by the unsteady dynamics of the flame observed during operation. With reduction in Kr concentration, only the core of fresh reactants is visible and details of the flame structure cannot be observed. These tomographic reconstructions were obtained from one acquisition, and – apart from flame A1 – spatial variations are observable in the reconstructed images. This is a consequence of the low photon flux of laboratory X-ray sources. For practical applications, increasing SNR can be addressed by increasing the number of tomographic acquisitions, and this aspect is further investigated in Section 4.3.3.

4.3.2. Equivalence ratio

To examine effects of equivalence ratio on the flame, flame series B is considered, in which the equivalence ratio is successively increased while holding the Kr mole fraction and Reynolds num-

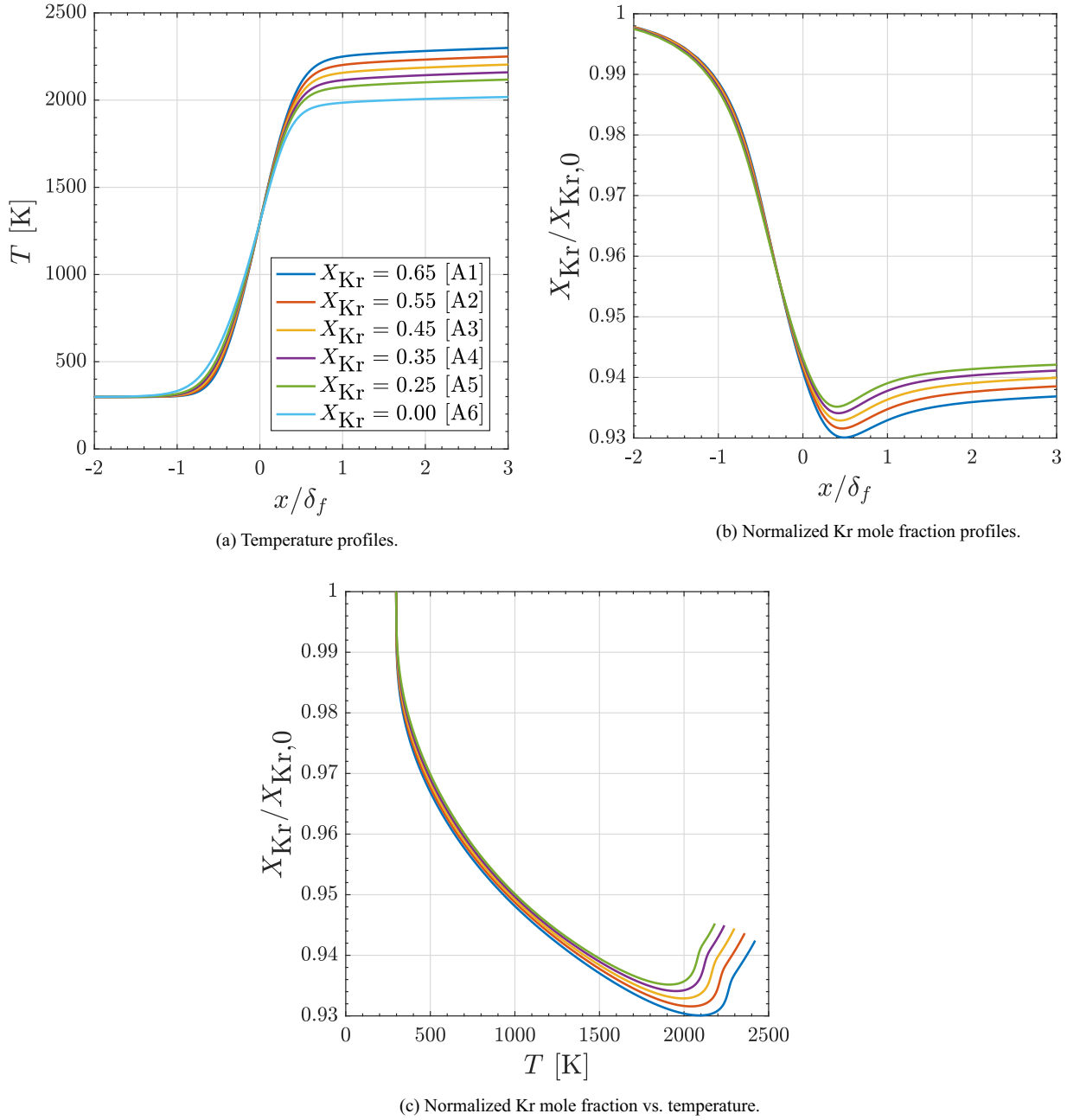


Fig. 6. Axial profiles of (a) temperature and (b) normalized Kr mole fraction along the 1D spatial coordinate x normalized by the flame thickness δ_f for unstrained laminar premixed flames A1–A6 simulated with CANTERA, and (c) normalized Kr mole fraction as a function of flame temperature.

ber constant. Reconstructed slices from one tomographic acquisition, consisting of a full 360° rotation and 1024 projection images, are shown in Fig. 8. It can be seen that with increasing equivalence ratio (from $\phi = 1.3$ (B1) to $\phi = 1.7$ (B5)) both the flame height h and the flame thickness δ_f continuously increase. These flame parameters can be estimated as [31].

$$h \approx \frac{U_j D}{2s_L}, \quad \delta_f \approx \frac{\alpha}{s_L}, \quad (14)$$

where U_j is the bulk flow velocity, D is the diameter of the jet, and α is the mean thermal diffusivity of the flame. Hence the reduction in flame speed by a factor of three between Flame B1 ($s_L = 48.9$ cm/s) and Flame B5 ($s_L = 15.9$ cm/s) is consistent with the observed trends, further validating the potential use of XCT in capturing the global flame behavior.

4.3.3. Statistical convergence of CT acquisitions

Statistical convergence and effects of averaging over multiple acquisitions were quantified by considering an additional experiment, in which flame C1 was operated ($Re = 462$, $\phi = 1.4$ and $X_{Kr} = 0.55$), collecting a total of 45 tomographic acquisitions at an angular resolution of 1.4° ($N_p = 256$ projection images per acquisition). Tomographic reconstructions from the average of $N_a = \{1; 15; 45\}$ acquisitions are presented in Fig. 9. Significant improvements in SNR were observed as the number of acquisitions increases. Further averaging in the azimuthal direction is investigated for $N_p = \{256; 11,520\}$ projection images in Fig. 9d and e.

The dependence of the reconstruction error and SNR on the number of acquisitions is estimated using the data inside the region delineated by the black lines in Fig. 9c. Results are shown in Fig. 10. It is first confirmed that performing the averaging before

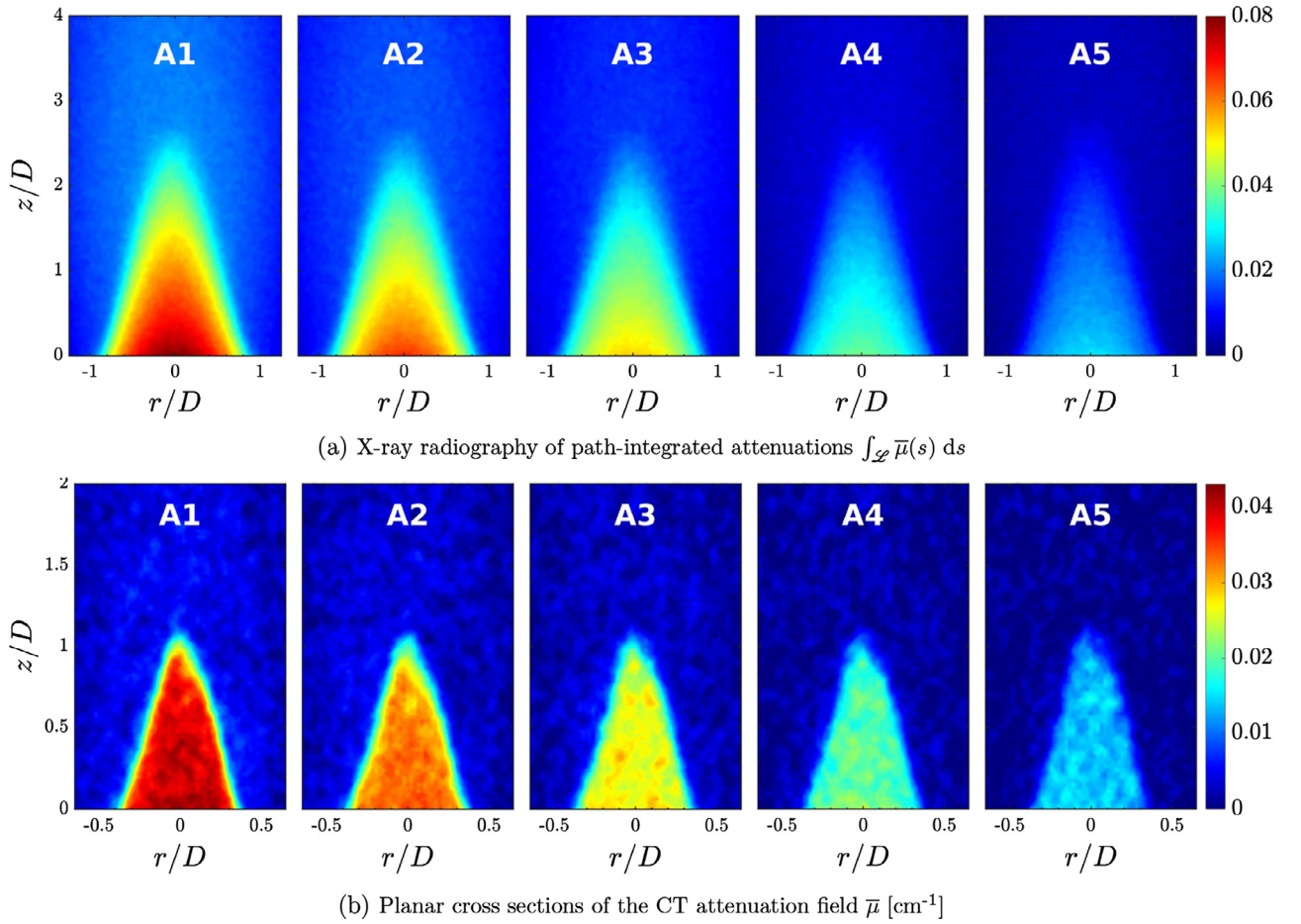


Fig. 7. (a) Radiography showing 2D projections of the entire flame and (b) CT reconstruction of a 2D center plane for different Kr mole fractions (see Table 1). Spatial resolution is 388 μm for radiography, 222 μm for tomography; results were obtained from 1024 projection images of one tomographic acquisition.

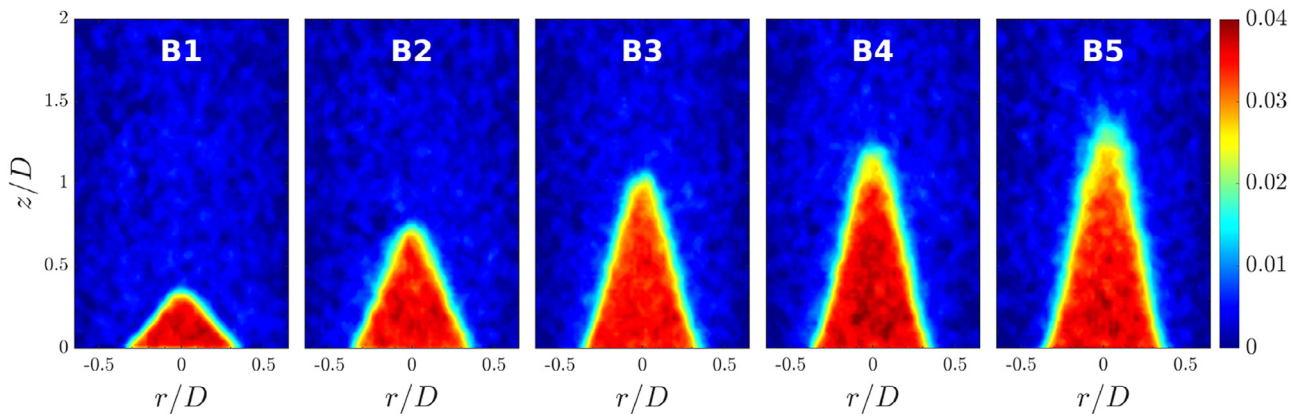


Fig. 8. Planar cross sections of the CT attenuation field $\bar{\mu}$ [cm^{-1}] for different equivalence ratios (Table 1). Results were acquired from 1024 projection images of one tomographic acquisition and reconstructed with a spatial resolution of 222 μm .

or after reconstruction yielded similar results, which is consistent with the linearity of the reconstruction algorithm around the beam center discussed in Section 3.4. It can be seen that the SNR increases with the number of acquisitions in reasonable correspondence with the theoretically expected rate of $N_a^{-1/2}$ for $N_a > 15$. In regard to the feasibility of acquiring a large number of scans, we note that the acquisition of a total of 256 projection images required less than 18 seconds and was limited by the detector to 15 images per second.

4.3.4. Comparison with numerical simulations

Detailed numerical simulations are performed to provide comparisons with the inferred flame structure from XCT measurements. For this, flame A1 is considered with the operating conditions specified in Table 1. Simulations are performed on a two-dimensional axisymmetric domain, extending 10D in the axial direction and 5D in the radial direction. The mesh was refined in the flame region using a grid spacing of 50 μm .

The governing equations describing conservation of mass, species, and momentum were solved using a low-Mach number

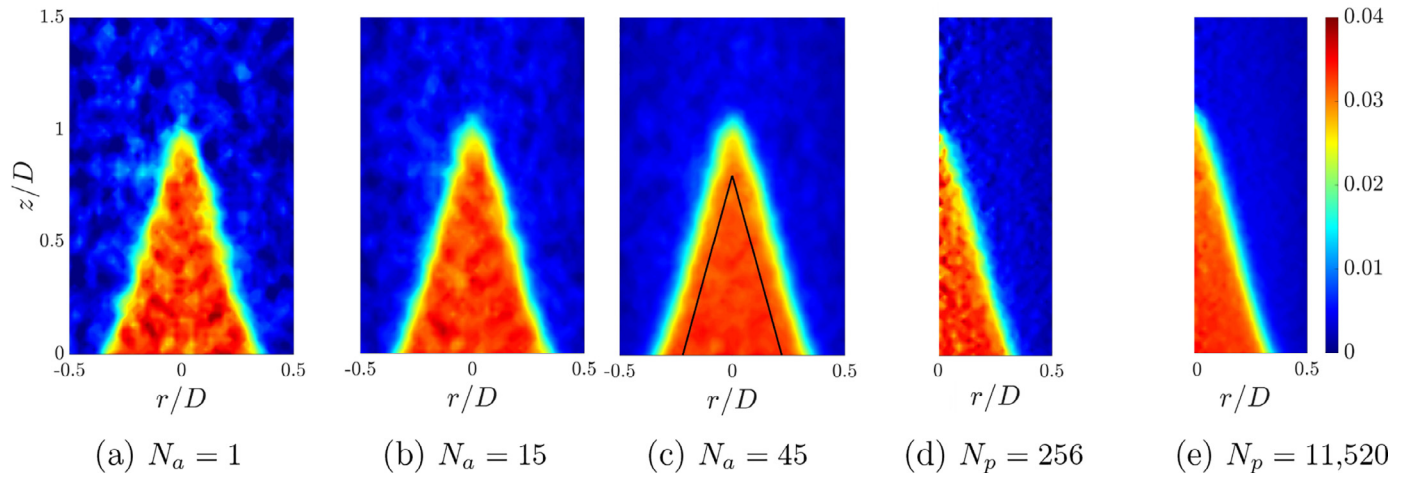


Fig. 9. Planar profile of the CT attenuation field $\bar{\mu}$ [cm^{-1}]. The results were averaged over $N_a = \{1; 15; 45\}$ acquisitions. (a), (b) and (c) are cross sections, while (d) and (e) are azimuthally averaged results over $N_p = \{256; 11,520\}$ projection images. Spatial resolution is $222\mu\text{m}$. The black lines in (c) delineates the region used to estimate SNR in Fig. 10.

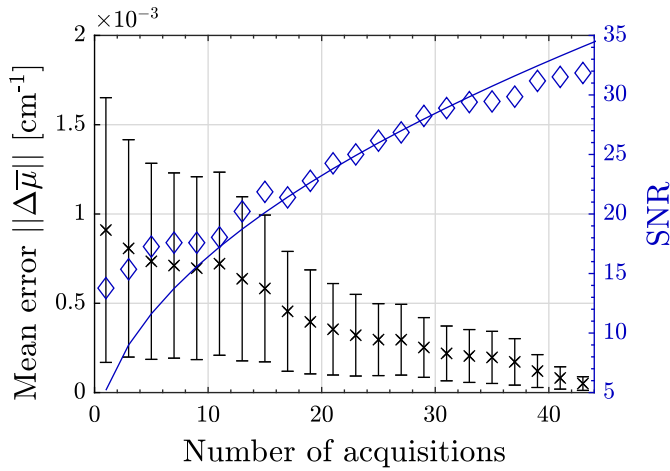


Fig. 10. Reconstruction error (crosses) and SNR (diamonds) of the CT attenuation field $\bar{\mu}$ with a theoretical square-root best-fit (full line). The error $\Delta\bar{\mu} = \bar{\mu} - \bar{\mu}_{\text{ref}}$ was estimated using a reference field $\bar{\mu}_{\text{ref}}$ obtained by averaging over 45 tomographic acquisitions. Vertical error bars indicate the standard deviation of the voxel distribution considered for averaging.

variable-density solver, with a second-order accurate finite difference discretization. The reaction chemistry was described using a 22-species mechanism, which was reduced from the modified GRI 3.0 mechanism discussed in Section 4.2 [32]. A second-order Strang-splitting scheme was applied to separate the convection, diffusion, and reaction operators. The reaction chemistry was integrated using an implicit backward differentiation scheme. The inlet velocity profile was retrieved from the measurements by relating the local flame angle to axial velocity and flame speed. The so computed nearly parabolic profile was prescribed with a bulk velocity of 0.62 m/s . A mild coflow of air with a velocity of 0.01 m/s was provided. The nozzle walls were considered to be adiabatic, and gravitation was included to account for negative buoyancy effects of the krypton gas.

Results are presented in Fig. 11, showing direct comparisons of planar measurements (left) and simulations (right) for (a) partial Kr density, (b) simulated temperature field and measured chemiluminescence, (c) inferred temperature T^* , as well as (d) simulated Kr mass fraction. From these results, it can be seen that the simulation captures the experimental flame height and flame shape to good accuracy. However, the measurements show a broadening

of the flame front. These discrepancies are attributed to observed unsteadiness of the flame brush during operation, an effect which was not represented by the simulation. Furthermore, given the limited resolution of the X-ray system of $388\mu\text{m}$ at the detector, corresponding to $222\mu\text{m}$ at the object, the location of the flame front is expected to be sensitive to such unsteadiness. Possible options for mitigating these issues are discussed in Section 5.

Figure 11d shows that with increasing downstream direction, Kr mixes with ambient air by entrainment. However, in the vicinity of the inner flame, the Kr field is rather uniform, and the flow density and temperature can thus locally be estimated from the partial Kr-density. Corresponding temperature comparisons are presented in Fig. 11c, in which the inferred temperature, as defined in Eq. (6), is reported for both the experimental and simulation results. The inferred temperature was also computed from the simulated Kr density, and can be compared to the simulated temperature field presented in Fig. 11b. These results highlight that inferring the temperature and density from the attenuation field yields plausible results in the fuel-rich inner flame, but is limited in the outer region of the flame as a consequence of the entrainment and reduced density of hot gases. The use of a coflow of tracer gas to mitigate this effect is discussed in Section 4.4.

To illustrate the use of XCT diagnostics for quantitative flow measurements, radial profiles of partial Kr density were extracted along three axial locations and are shown in Fig. 12. It can be seen that the Kr density is well estimated from the XCT signal using $N_a = 10$ acquisitions, even if the broadening of the flame already observed in Fig. 11 also appears in this quantitative comparison.

4.4. Extension to geometrically complex flame

The reacting flow results presented so far were obtained using an axi-symmetric Bunsen flame. In this section, a more complex flame geometry is analyzed using XCT. For this, a burner was designed with a S-shaped inlet, and the experimental configuration of this burner is illustrated in Fig. 1c. A quartz tube of inner diameter 57.0 mm and 2.0 mm thickness was placed around the burner to confine the flame, and a coflow was supplied consisting of a Kr/air mixture that matches the Kr mole fraction of the fuel stream. The primary flow was operated with a similar mixture as the Bunsen flame, with a bulk flow velocity of 0.771 m/s , an equivalence ratio of 1.30 and a Kr mole fraction of 0.65 . The flow diagram in Fig. 1a shows that the coflow was derived from the primary flow using

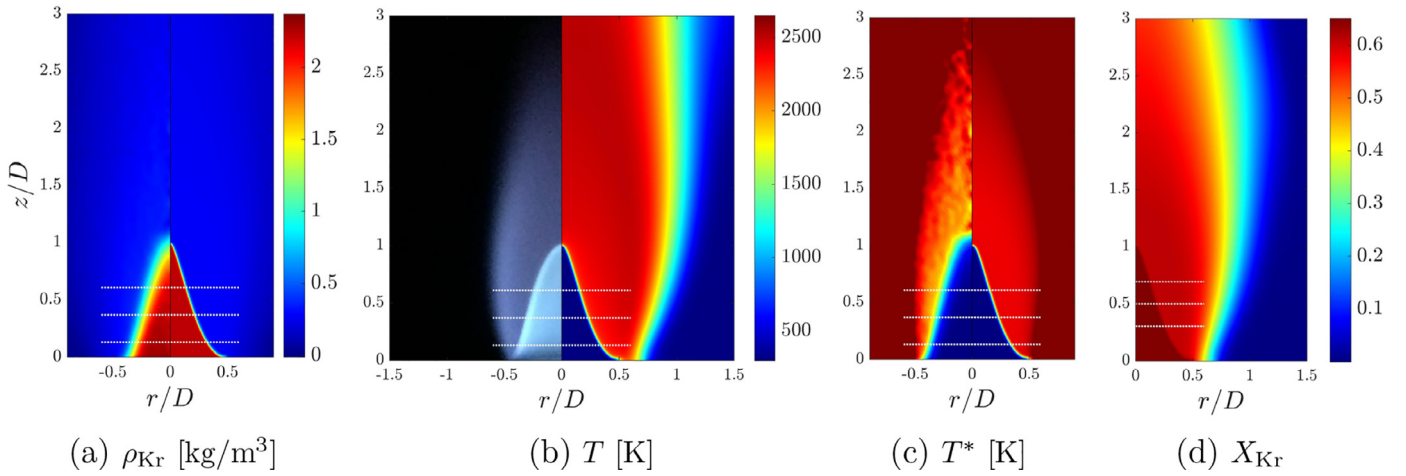


Fig. 11. Comparisons of measurements (left panels) with numerical simulations (right panels) for (a) partial Kr density, (b) chemiluminescence from experiment and simulated temperature, (c) inferred temperature T^* , and (d) simulated Kr mole fraction. All results are shown along a center plane through the flame, and the XCT results were obtained by averaging over ten tomographic acquisitions. The dashed white lines indicate the locations of the density profiles plotted in Fig. 12.

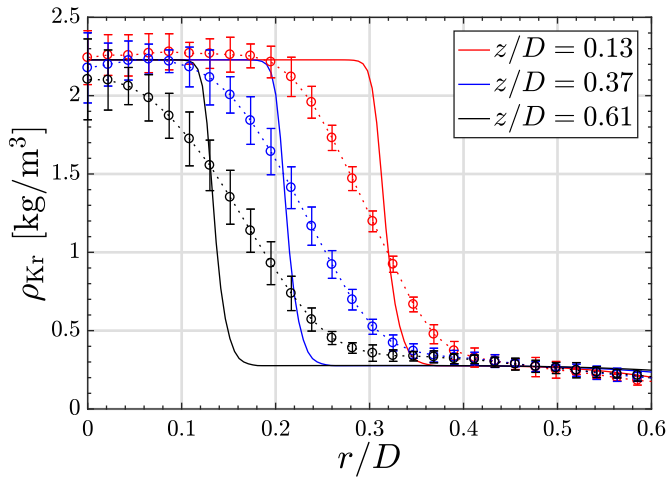


Fig. 12. Comparisons of radial profiles of Kr density between experiments (dashed lines with symbols) and simulations (solid lines) at three axial locations. Vertical error bars on the density are inferred from the voxel-wise standard deviation over ten acquisitions.

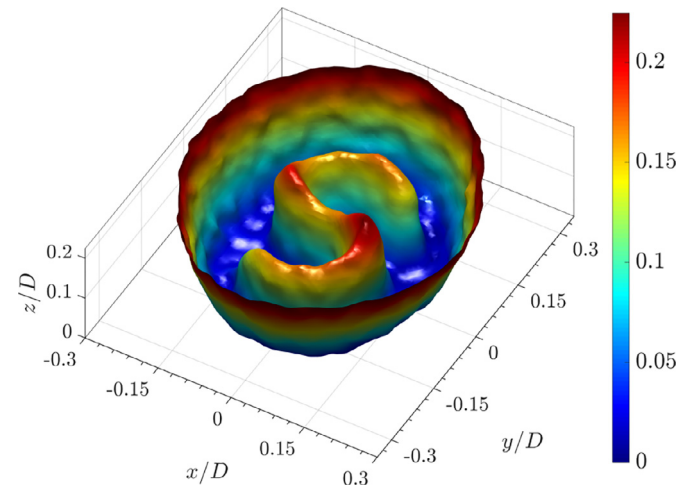


Fig. 13. 3D representation of the S-flame reconstructed by XCT. The isocontour at a temperature of 1200 K is shown and colored by the relative height z/D with respect to the burner. (For interpretation of the references to color in this figure legend, the reader is referred to the web version of this article.)

a T-junction placed upstream of a check valve and the methane junction, and was regulated to a bulk flow velocity of 4.0 cm/s. This composition thus corresponded to a $\text{Kr}/\text{O}_2/\text{air}$ mixture with a Kr mole fraction of 0.74. It was used to create an environment of uniform Kr concentration around the flame to facilitate temperature evaluations in the two-stream system. Similar to the Bunsen flame, by assuming a uniform concentration of Kr, an inferred temperature field T^* was retrieved. Ten acquisitions of $N_p = 640$ projection images per 360° rotation of the object were acquired, averaged and reconstructed following the same procedure as for the Bunsen flame.

CT results are presented in Figs. 13–15 showing the attenuation μ and inferred temperature T^* fields. In these figures, the diameter $D = 57.0 \text{ mm}$ of the surrounding quartz tube is used to normalize the spatial coordinates. Figure 13 shows a 3D isocontour at a temperature of 1200 K, colored by the relative height z/D with respect to the burner exit. Two surfaces can be identified, namely the interface, shaped like an S, between the fresh gases from the primary flow and the inner flame, and the interface between the outer region of the flame and the fresh gases from the secondary

flow. Figures 14 and 15 present three planar cross sections of the CT reconstructed attenuation and inferred temperature.

Given the resolution of 388 μm at the detector, the width of the flame corresponds to approximately 50 pixels. This is still sufficient to qualitatively retrieve the shape of the flame, and to obtain well converged results in the fresh-gas region. The attenuation signal in the hot-gas region is noisier due to the low-density gas stream. However, compared to the Bunsen flame the temperature in the outer region of the flame is well captured, which is due to the surrounding coflow and the rather uniform Kr environment. This confirms the potential of using a tracer-gas coflow to extend CT measurements of partial density for reliably obtaining temperature.

5. Discussion of potential improvements

In the previous sections, limitations of XCT were identified. This section offers a further discussion of these limitations along with potential improvements. Increasing the spatial resolution and signal intensity are first investigated before examining potential alternatives for modifying the spectral characteristics of the X-ray system.

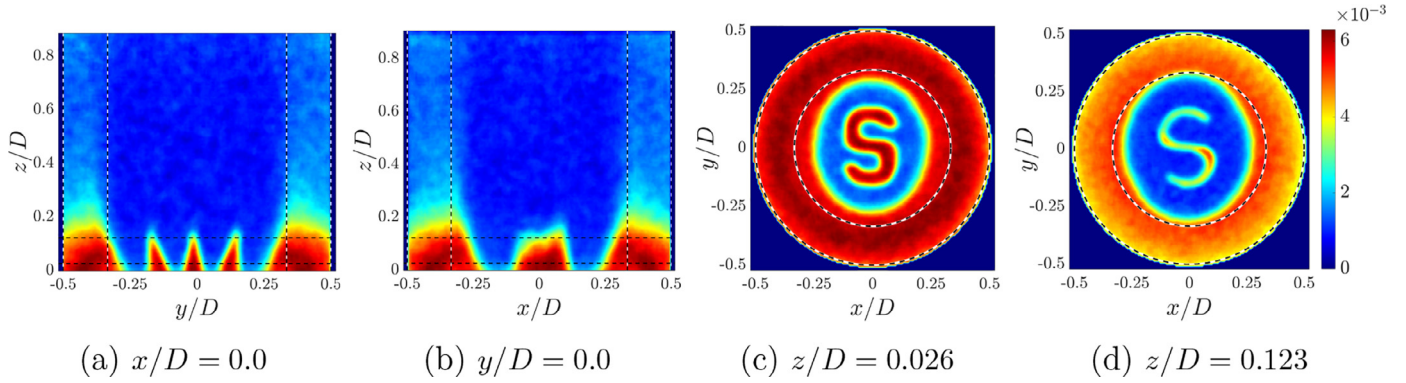


Fig. 14. Planar cross sections of the attenuation field $\bar{\mu}$ [cm^{-1}] of the S-flame reconstructed by XCT. The black and white dashed lines indicate the diameters of the burner mount (38.1 mm) and the surrounding quartz tube ($D = 57.0$ mm). The horizontal black dashed lines in (a) and (b) indicate the heights of the cross sections (c) and (d).

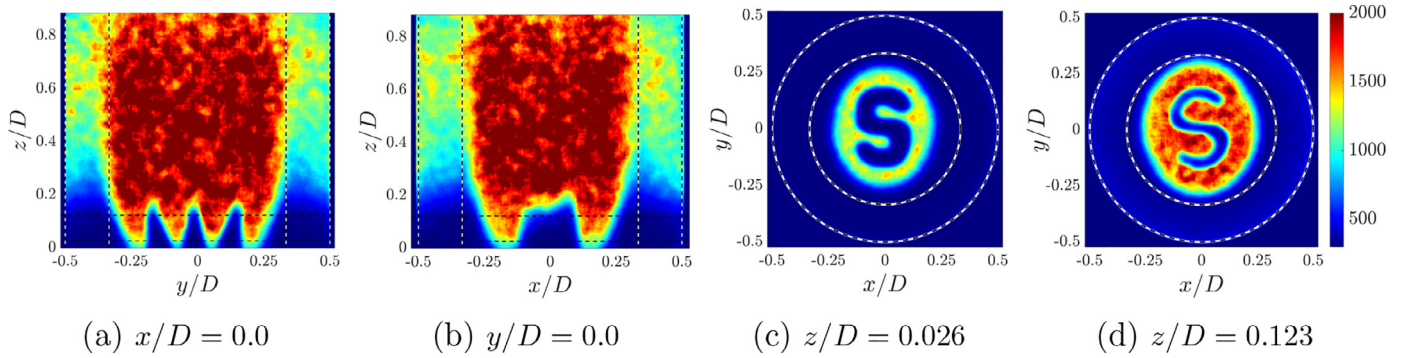


Fig. 15. Planar cross sections of the inferred temperature field T^* [K] of the S-flame reconstructed by XCT. The black and white dashed lines indicate the diameters of the burner mount (38.1 mm) and the surrounding quartz tube ($D = 57.0$ mm). The horizontal black dashed lines in (a) and (b) indicate the heights of the cross sections (c) and (d).

5.1. Increasing the spatial resolution

A first limitation identified in this work is the spatial resolution of the present setup. It is possible to leverage the conical geometry of the beam in order to increase the magnification of the object and increase the spatial resolution. Such a procedure was recently employed to visualize cavitation phenomena in diesel flows with a geometric magnification of ten times and a voxel resolution of $15\text{ }\mu\text{m}$ using micro-CT [33]. However, doing so requires using micro-focus sources, which feature focal spot sizes of the order of $1\text{ }\mu\text{m}$. Applying this procedure to gas-phase tomography was not directly implementable in the current setup, and remains the subject of future work. It should be noted that due to the lower photon count by micro-focus sources, the acquisition time is expected to increase appreciably.

In the present setup, the magnification and resolution were limited because of the nominal focal spot size of 0.3 mm , resulting in blurred results when considering resolutions lower than this value. Another aspect to consider is the rotation of the sample. In the current setup, the burner is rotated continuously. To prevent blurring of points of the object over several pixels, further refining the resolution would require step-wise rotation.

5.2. Signal intensity and statistical convergence

Sufficient statistical convergence was observed in cold-gas regions but appreciable noise was encountered for the burnt gases due to the reduction in attenuation by up to a factor of eight. This reduction in attenuation intensity can be addressed by increasing the number of projections, increasing the photon count, exposure time, or increasing the radiodensity of the tracer gas, for instance

by using xenon. This is highlighted by the following relation for SNR [19,34]

$$\text{SNR} \propto \frac{\bar{\mu}_i}{\sigma} \propto \frac{pW_iX_i\bar{\zeta}_i}{R_uT} \sqrt{N_p I_T w^2 \tau}, \quad (15)$$

where σ is the standard deviation in the signal, N_p is the number of projections, I_T is the tube intensity, w is the detector pixel size, and τ is the exposure time.

5.3. Spectral considerations and X-ray systems

Although Kr is a rare gas, at the highest considered Kr flow rate of 0.03 L/s , one acquisition required less than 2 L of Kr, thus keeping this diagnostic affordable. It was experimentally observed that no signal was distinguishable with the present setup when using less radiodense Ar as a more affordable alternative to Kr. Indeed, radiography systems, such as the one used in this work, are designed to operate in the $40\text{--}150\text{ kVp}$ tube energy range. Due to the embedded filtration, equivalent to 3 mm of Al in this work, the low energy part of the spectrum, including the target material characteristic lines, are highly attenuated. Typical emission spectra of radiography sources from the literature are presented by solid lines in Fig. 16 [35]. It can be seen that the attenuation of Ar is significantly lower than that of Kr in the range of photon energies emitted by a radiography source. Comparisons of spectra for 40 kVp and 55 kVp tube voltages, normalized at equivalent tube intensities, highlight that increasing the tube voltage generates more photons. However, since these systems are limited in power, operating at higher tube voltages directly implies operating at lower tube intensities, and the effect on SNR depends on the specific attenuation of the object.

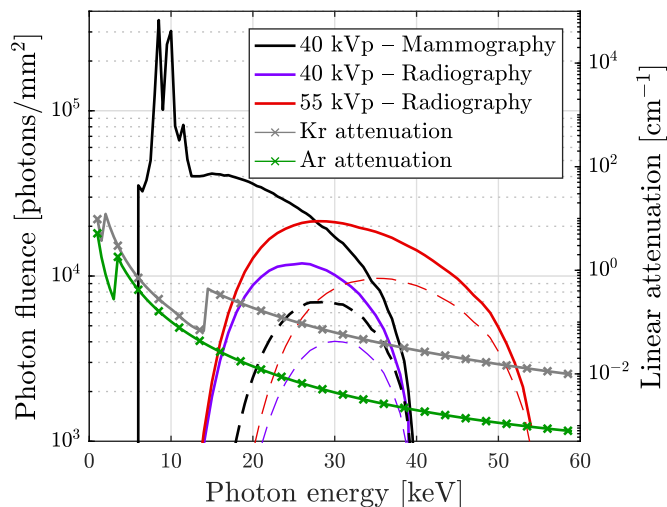


Fig. 16. Comparisons of theoretical spectra emitted by mammography and radiography X-ray tubes with W target. Full lines represent unfiltered spectra, while the dashed lines are obtained with a theoretical filter of 4 mm of SiO_2 . The linear attenuation $\mu(E)$ of pure Kr and Ar gases at ambient conditions are plotted.

Further tuning of the X-ray spectrum represents an interesting opportunity in order to increase the intensity of the signal. Alternatives include dental or mammography CT systems used to image less attenuating tissues than radiography systems. Mammography CT systems usually operate in the 20–40 kVp energy range with tube targets made of tungsten, molybdenum or rhodium [36]. The spectra of a mammography system is compared with radiography systems in Fig. 16 highlighting the potential increase in signal for systems with optical access. Indeed, the X-ray attenuation is higher at lower energies and the K-edge of the Kr attenuation at 14.3 keV matches with the characteristic X-ray emission lines of typical target materials, which include most of the spectral energy: about 30 lines between 7.6 and 12.1 keV for tungsten, 2 K-edge lines at 17.4 and 19.6 keV for molybdenum, and 2 K-edge lines at 20.2 and 22.7 keV for rhodium. Furthermore, theoretical calculations based on these spectra suggest that, under the condition that no filtration is added, a signal of equivalent intensity as the one from radiography employed in the present work can be achieved by using a mammography X-ray system and Ar as a tracer gas. These theoretical observations were not verified experimentally as the required hardware was not available, nor directly implementable on the considered system.

Radiography sources generate more penetrating photons, and are therefore interesting alternatives for applications to optically inaccessible flows. The optimal SNR ratio for the enclosed S-flame was obtained for a tube voltage of 55 kVp, a value beyond the range of typical mammography sources. To illustrate this further, the effect of adding a filtration of 4 mm of SiO_2 , emulating the absorption of the quartz tube used around the S-flame, was theoretically estimated [21] and the obtained spectra for mammography and radiography sources are plotted with dashed lines in Fig. 16. Because of the absorption by the quartz tube, the low-energy photons generated by the mammography system are less penetrating and therefore more attenuated. To overcome these limitations, photon-counting detectors and dual-energy X-ray absorption offer interesting alternatives for improving the accuracy of gas-phase measurements [37].

6. Conclusions

This work examined the feasibility of employing laboratory X-ray systems for absorption measurements of gas-phase combus-

tion through radiography and computed tomography. To this end, two premixed laminar flames were examined and operated with methane/air mixtures diluted with Kr as a radiodense tracer-gas. Effects of tracer gas concentration, operating conditions, and number of acquisitions on the quantitative extraction of density and temperature fields were examined. These experimental investigations were complemented by numerical simulations to enable quantitative comparisons with measurements.

From this study, it was found that SNR is a function of tracer gas concentration, scanner-setting, and number of acquisitions. For the example of a Bunsen burner flame at steady-state with a Kr mole fraction of 0.55, a maximum SNR of 32 was obtained by averaging over 45 tomographic acquisitions of 256 projection images, each acquisition requiring 18 s, making this a viable technique for rapid data collection.

Analysis of the measurements showed that the tomographic reconstructions captured expected trends in flame characteristics, such as the dependence of the flame height and flame thickness on equivalence ratio and Kr dilution. A method for extracting the gas temperature from linear attenuation data was developed and applied to measurements, showing qualitative agreement with detailed numerical simulations, and quantitative results were obtained for gas density. The uncertainties of these results due to variations in Kr mole fraction across the flame and fluctuations in measured attenuation were discussed. Using a non-axisymmetric S-flame confined in a quartz tube, the diagnostics was further applied to more complicated geometries without direct optical access. The use of a coflow of tracer gas to provide a uniform tracer gas environment was shown to improve the evaluation of gas temperature.

Despite the inherent limitations of laboratory X-ray systems in regard to spatial resolution and photon flux, their accessibility and robust operation make them an attractive diagnostic for flame imaging in optically inaccessible media. Energy-discriminating detectors, advanced post-processing methods, as well as synchrotron X-ray sources with significantly higher fluxes, spatial resolutions, and acquisition rates, provide further opportunities for improving the accuracy of gas-phase combustion measurements.

Acknowledgments

This work was supported by a Leading Edge Aeronautics Research for NASA (LEARN) grant (Award no. [NNX15AE42A](#)) and by the National Science Foundation (Award No. [CBET-1800906](#) and Graduate Research Fellowship with No. 1656518). The X-ray system used was purchased thanks to a NIH S10 shared instrument grant (No. [S10RR026714-01](#)). Jared Dunn is acknowledged for devising an early Bunsen-burner experiment. The authors would like to thank Robert Bennett for helping with setting up the X-ray system. Dula Parkinson and Harold Barnard are acknowledged for their valuable input on experimental and reconstruction methods for computed tomography.

References

- [1] R.J. Santoro, H.G. Semerjian, P.J. Emmerman, R. Goulard, Optical tomography for flow field diagnostics, *Int. J. Heat Mass Transf.* 24 (7) (1981) 1139–1150.
- [2] L. Ma, W. Cai, A.W. Caswell, T. Kraetschmer, S.T. Sanders, S. Roy, J.R. Gord, Tomographic imaging of temperature and chemical species based on hyperspectral absorption spectroscopy, *Opt. Express* 17 (10) (2009) 8602–8613.
- [3] W. Cai, C.F. Kaminski, Tomographic absorption spectroscopy for the study of gas dynamics and reactive flows, *Prog. Energy Combust. Sci.* 59 (2017) 1–31.
- [4] J. Floyd, A.M. Kempf, Computed tomography of chemiluminescence (CTC): high resolution and instantaneous 3-D measurements of a matrix burner, *Proc. Combust. Inst.* 33 (2011) 751–758.
- [5] K. Mohri, S. Görs, J. Schöler, A. Rittler, T. Dreier, C. Schulz, A. Kempf, Instantaneous 3D imaging of highly turbulent flames using computed tomography of chemiluminescence, *Appl. Opt.* 56 (26) (2017) 7385–7395.

- [6] A. Schwarz, Multi-tomographic flame analysis with a schlieren apparatus, *Meas. Sci. Technol.* 7 (1996) 406–413.
- [7] A.K. Agrawal, N.K. Butuk, S.R. Gollahalli, D. Griffin, Three-dimensional rainbow schlieren tomography of a temperature field in gas flows, *Appl. Opt.* 37 (3) (1998) 479–485.
- [8] A. Kastengren, C.F. Powell, Synchrotron X-ray techniques for fluid dynamics, *Exp. Fluids* 55 (2014) 1686.
- [9] A.G. MacPhee, M.W. Tate, C.F. Powell, Y. Yue, M.J. Renzi, A. Ercan, S. Narayanan, E. Fontes, J. Walther, J. Schaller, S.M. Gruner, J. Wang, X-ray imaging of shock waves generated by high-pressure fuel sprays, *Science* 295 (5558) (2002) 1261–1263.
- [10] A. Kastengren, C.F. Powell, Y.J. Wang, K.S. Im, J. Wang, X-ray radiography measurements of diesel spray structure at engine-like ambient density, *Atom. Sprays* 19 (11) (2009) 1031–1044.
- [11] B.R. Halls, C.D. Radke, B.J. Reuter, A.L. Kastengren, J.R. Gord, T.R. Meyer, High-speed, two-dimensional synchrotron white-beam X-ray radiography of spray breakup and atomization, *Opt. Express* 25 (2) (2017) 1605–1617.
- [12] A. Kastengren, C.F. Powell, E.M. Dufresne, D.A. Walko, Application of X-ray fluorescence to turbulent mixing, *J. Synchrotron Rad.* 18 (5) (2011) 811–815.
- [13] S.A. Schumaker, A.L. Kastengren, S.D. Danczyk, M.L. Lightfoot, X-ray fluorescence measurements of turbulent methane-oxygen shear coaxial flames, in: 9th US National Combustion Meeting, no. 114DI-0074, Cincinnati, OH, 2015.
- [14] N. Hansen, R.S. Tranter, K. Moshhammer, J.B. Randazzo, J.P. Lockhart, P.G. Fugazzi, T. Tao, A.L. Kastengren, 2d-imaging of sampling-probe perturbations in laminar premixed flames using Kr X-ray fluorescence, *Combust. Flame* 181 (2017) 214–224.
- [15] R.S. Tranter, A.L. Kastengren, J.P. Porterfield, J.B. Randazzo, J.P.A. Lockhart, J.H. Baraban, G.B. Ellison, Measuring flow profiles in heated miniature reactors with x-ray fluorescence spectroscopy, *Proc. Combust. Inst.* 36 (3) (2017) 4603–4610.
- [16] B. Hasçakir, G. Glatz, L.M. Castanier, A. Kovscek, In-situ combustion dynamics visualized with X-ray computed tomography, *SPE J.* 16 (3) (2011) 524–536.
- [17] F. Coletti, M.J. Benson, A.L. Sagues, B.H. Miller, R. Fahrig, J.K. Eaton, Three-dimensional mass fraction distribution of a spray measured by X-ray computed tomography, *J. Eng. Gas Turbines Power* 136 (5) (2014) 051508.
- [18] J. Dunnmon, S. Sobhani, T.W. Kim, A. Kovscek, M. Ihme, Characterization of scalar mixing in dense gaseous jets using X-ray computed tomography, *Exp. Fluids* 56 (193) (2015) 1–17.
- [19] J. Dunnmon, S. Sobhani, M. Wu, R. Fahrig, M. Ihme, An investigation of internal flame structure in porous media burners using X-ray computed tomography, *Proc. Combust. Inst.* 36 (2017) 4399–4408.
- [20] J. Als-Nielsen, D. McMorrow, *Elements of modern X-ray physics*, John Wiley & Sons, 2011.
- [21] J.H. Hubbell, S.M. Seltzer, Tables of X-ray mass attenuation coefficients and mass energy-absorption coefficients 1 keV to 20 MeV for elements $Z = 1$ to 92 and 48 additional substances of dosimetric interest, 1995. Technical report
- [22] J. Hsieh, *Computed tomography: principles, design, artifacts, and recent advances*, 3rd ed., SPIE Press, 2015.
- [23] A. Kyrieles, V. Titarenko, M. Ibison, T. Connolly, P.J. Withers, Region-of-interest tomography using filtered backprojection: assessing the practical limits, *J. Microsc.* 241 (1) (2010) 69–82.
- [24] L.A. Feldkamp, L.C. Davis, J.W. Kress, Practical cone-beam algorithm, *J. Opt. Soc. Am. A* 1 (6) (1984) 612–619.
- [25] W. van Aarle, W.J. Palenstijn, J. Cant, E. Janssens, F. Bleichrodt, A. Dabavolski, J.D. Beenhouwer, K.J. Batenburg, J. Sijbers, Fast and flexible X-ray tomography using the ASTRA toolbox, *Opt. Express* 24 (22) (2016) 25129–25147.
- [26] J.L. Prince, J.M. Links, *Medical imaging signals and systems*, Pearson Prentice Hall, 2006.
- [27] G.N. Ramachandran, A.V. Lakshminarayanan, Three-dimensional reconstruction from radiographs and electron micrographs: application of convolutions instead of Fourier transforms, *Proc. Natl. Acad. Sci. USA* 68 (9) (1971) 2236–2240.
- [28] D.G. Goodwin, H.K. Moffat, R.L. Speth, *Cantera: An object-oriented software toolkit for chemical kinetics, thermodynamics, and transport processes*, 2017, <http://www.cantera.org>, version 2.3.0.
- [29] G.P. Smith, D.M. Golden, M. Frenklach, N.W. Moriarty, B. Eiteneer, M. Goldenberg, C.T. Bowman, R.K. Hanson, S. Song, W.C. Gardiner Jr, V.V. Lissianski, Z. Qin, *GRI-mech 3.0*, 2000, <http://www.me.berkeley.edu/gri-mech/>.
- [30] J.O. Hirschfelder, C.F. Curtiss, R.B. Bird, *Molecular theory of gases and liquids*, John Wiley & Sons, 1969.
- [31] C.K. Law, *Combustion physics*, Cambridge University Press, 2006.
- [32] T. Jaravel, E. Riber, B. Cuenot, G. Bulat, Large eddy simulation of an industrial gas turbine combustor using reduced chemistry with accurate pollutant prediction, *Proc. Combust. Inst.* 36 (2017) 3817–3825.
- [33] N. Mitroglou, M. Lorenzi, M. Santini, M. Gavaises, Application of x-ray micro-computed tomography on high-speed cavitating diesel fuel flows, *Exp. Fluids* 57 (11) (2016) 1–14.
- [34] A. Macovski, *Medical imaging systems*, Prentice Hall, 1983.
- [35] A. Sisniega, M. Desco, J.J. Vaquero, Modification of the TASMIP x-ray spectral model for the simulation of microfocus x-ray sources, *Med. Phys.* 41 (1) (2013) 011902.
- [36] J.M. Boone, T.R. Fewell, R.J. Jennings, Molybdenum, rhodium, and tungsten anode spectral models using interpolating polynomials with application to mammography, *Med. Phys.* 24 (12) (1997) 1863–1874.
- [37] M. Persson, B. Huber, S. Karlsson, X. Liu, H. Chen, C. Xu, M. Yveborg, H. Bornefalk, M. Danielsson, Energy-resolved CT imaging with a photon-counting silicon-strip detector, *Phys. Med. Biol.* 59 (22) (2014) 6709–6727.